



HAL
open science

Crystal Growth Promotion and Defect Passivation by Hydrothermal and Selenized Deposition for Substrate-Structured Antimony Selenosulfide Solar Cells

Guo-Jie Chen, Rong Tang, Shuo Chen, Zhuang-Hao Zheng, Zhenghua Su, Hong-Li Ma, Xianghua Zhang, Ping Fan, Guang-Xing Liang

► To cite this version:

Guo-Jie Chen, Rong Tang, Shuo Chen, Zhuang-Hao Zheng, Zhenghua Su, et al.. Crystal Growth Promotion and Defect Passivation by Hydrothermal and Selenized Deposition for Substrate-Structured Antimony Selenosulfide Solar Cells. *ACS Applied Materials & Interfaces*, 2022, 14 (28), pp.31986-31997. 10.1021/acsami.2c06805 . hal-03773013

HAL Id: hal-03773013

<https://hal.science/hal-03773013>

Submitted on 15 Jun 2023

HAL is a multi-disciplinary open access archive for the deposit and dissemination of scientific research documents, whether they are published or not. The documents may come from teaching and research institutions in France or abroad, or from public or private research centers.

L'archive ouverte pluridisciplinaire **HAL**, est destinée au dépôt et à la diffusion de documents scientifiques de niveau recherche, publiés ou non, émanant des établissements d'enseignement et de recherche français ou étrangers, des laboratoires publics ou privés.

Crystal Growth Promotion and Defects Passivation by Hydrothermal and Selenized Deposition for Substrate Structured Antimony Selenosulfide Solar Cells

Guo-Jie Chen¹, Rong Tang¹, Shuo Chen¹, Zhuang-Hao Zheng¹, Zheng-Hua Su¹, Hong-Li Ma², Xiang-Hua Zhang², Ping Fan^{1,3}, Guang-Xing Liang^{*1}

¹*Shenzhen Key Laboratory of Advanced Thin Films and Applications, Key Laboratory of Optoelectronic Devices and Systems of Ministry of Education and Guangdong Province, College of Physics and Optoelectronic Engineering, Shenzhen University, Shenzhen, 518060, P. R. China*

²*Univ Rennes, CNRS, ISCR (Institut des Sciences Chimiques de Rennes) UMR 6226, Rennes, F-35000, France*

³*Shenzhen University Institute of Microscale Optoelectronics, Shenzhen University, Shenzhen, 518060, P. R. China*

*Corresponding author, E-mail: lgx@szu.edu.cn (Prof. Liang)

Keywords: Substrate structure; Post-selenization; Sb₂(S,Se)₃; Crystal growth; Defect passivation;

Abstract

Antimony sulfide-selenide ($\text{Sb}_2(\text{S},\text{Se})_3$) is a promising light-harvesting material for stable and high-efficiency thin-film photovoltaics (PV), because of its excellent light-harvesting capability, abundant elemental storage, and excellent stability. This study aimed to expand the application of $\text{Sb}_2(\text{S},\text{Se})_3$ solar cells with a substrate structure as a flexible or tandem device. The use of a hydrothermal method accompanied by a post-selenization process for the deposition of $\text{Sb}_2(\text{S},\text{Se})_3$ film based on the solar cell substrate structure was firstly demonstrated. The mechanism of post-selenization treatment on crystal growth promotion of $\text{Sb}_2(\text{S},\text{Se})_3$ film and the defect passivation of $\text{Sb}_2(\text{S},\text{Se})_3$ solar cell were revealed through different characterization methods. The crystallinity and the carrier transport property of the $\text{Sb}_2(\text{S},\text{Se})_3$ film improved, and both the interface defect density of $\text{Sb}_2(\text{S},\text{Se})_3/\text{CdS}$ interface and the bulk defect density of $\text{Sb}_2(\text{S},\text{Se})_3$ absorber decreased. Through these abovementioned processes, the transport and collection of electronics can be improved, and the defect recombination loss can be reduced. By using post-selenization treatment to optimize the absorber layer, $\text{Sb}_2(\text{S},\text{Se})_3$ solar cells with the configuration SLG/Mo/ $\text{Sb}_2(\text{S},\text{Se})_3$ /CdS/ITO/Ag achieved an efficiency of 4.05%. This work can provide valuable information for the further development and improvement of $\text{Sb}_2(\text{S},\text{Se})_3$ solar cells.

Introduction

Recently, thin-film photovoltaic (TFPV) technologies have received an increasing amount of attention due to their advantages of high flexibility and low material consumption and are considered successors to silicon-based PVs. For example, cadmium telluride (CdTe) and copper indium gallium selenide (CIGS) have not only achieved efficiency rates of up to 22.1% and 23.35% in the laboratory, respectively, but also showed a decent current market share and potential for industrialization.¹⁻² Nevertheless, the scarcity of In, Ga, and Te elements and the toxicity of Cd elements might hinder their further development. Thus, it is urgent to find some cost-effective, environmentally friendly, and intrinsically stable TFPV materials. Antimony chalcogenides $Sb_2(S_x,Se_{1-x})_3$ ($0 \leq x \leq 1$) have emerged as highly promising candidates owing to their excellent photoelectric properties.³⁻⁶ As a promising absorber, $Sb_2(S_x,Se_{1-x})_3$ has a tunable bandgap (1.1 – 1.7 eV), a remarkable absorption coefficient at visible light ($>10^5 \text{ cm}^{-1}$), excellent stability, and a low-toxicity component, which are essential for solar cells with high power conversion efficiency (PCE).⁷⁻⁹ Moreover, $Sb_2(S,Se)_3$ film has anisotropic electrical properties due to its stable single orthorhombic phase with a Q1D crystal structure.¹⁰⁻¹¹ Conductivity along the $(Sb_4X_6)_n$ ($X = S$ or Se) ribbons (c-axis) is much higher than in the other directions, which is beneficial for enhancing carrier transport and decreasing recombination losses; it is the intrinsic requirement for the high-efficiency solar cell.¹²⁻¹³ Over the past years, many methods have been developed to prepare $Sb_2(S,Se)_3$ absorber layers, such as vapor transport deposition (VTD), co-evaporation, and hydrothermal. Although the VTD and

co-evaporation methods have achieved impressive efficiency, these methods have plenty of problems.¹⁴⁻¹⁵ For instance, the vaporized intermediate particles during the deposition would most likely generate defects that affect efficiency.^{3, 16} In addition, the solution-processed (spin coating followed by annealing) $\text{Sb}_2(\text{S,Se})_3$ films demonstrate low crystallinity, which indicate low conductivity. Consequently, we adopted reactive hydrothermal deposition for the $\text{Sb}_2(\text{S,Se})_3$ film fabrication because of its outstanding advantage of low-cost, improved film morphology and reduced defect. Up to now, the reported device structure of $\text{Sb}_2(\text{S,Se})_3$ solar cells is divided into two types of structure: substrate and superstrate structures. The efficiency of the $\text{Sb}_2(\text{S,Se})_3$ solar cell based on superstrate structure via hydrothermal deposition method has achieved the highest efficiency of 10%.^{3, 7, 17} Considering the simple preparation process and ohmic contacts for the $\text{Sb}_2(\text{S,Se})_3$ layer, almost all the studies pay more attention to $\text{Sb}_2(\text{S,Se})_3$ solar cells with superstrate structure. However, the substrate configuration of solar cells also has many advantages. For example, it is beneficial for tailoring the absorber layer independently, improving the interface quality, and absorbing sunlight directly; it has a significant application on flexible and tandem solar cells.¹⁸⁻¹⁹ However, $\text{Sb}_2(\text{S,Se})_3$ thin-film solar cell with the substrate structure is rarely studied. Therefore, further study of the $\text{Sb}_2(\text{S,Se})_3$ thin-film solar cell with the substrate structure is needed. Past experience in well-developed photovoltaic technologies has demonstrated that post-treatment of light absorption materials is an effective method to optimize their crystallinity and electrical properties.^{17, 20} Each absorber material requires different post-treatments to control the grain growth and passivate defects. For instance, as for CIGS²¹⁻²², CdTe²³⁻

²⁴, and perovskite solar cells²⁵⁻²⁶, the post-treatment is quite distinct. Thus, it is a challenge to find suitable materials and appropriate post-treatment. The hydrothermal method as a useful method in film fabrication still has some shortcomings, such as weak crystallinity and preferred [hk0] orientation. The post-selenization process is the most common method, that can improve the crystallinity of the film, passivate the selenide vacancy, and suppress the recombination loss.²⁷⁻²⁸ Therefore, it is necessary to figure out the appropriate post-selenization treatment for the future development of highly efficient $\text{Sb}_2(\text{S,Se})_3$ thin-film solar cells.

In this work, we reported a post-selenization treatment for improving the performance of hydrothermal deposited $\text{Sb}_2(\text{S,Se})_3$ thin film and its solar cells. By carefully controlling the selenization process, we discovered that the post-selenization treatment enhanced the crystallinity and quality of the absorber layer and passivated the defect both in the bulk and at the interface, which jointly enabled the improvement of the FF and J_{SC} . Finally, we fabricated $\text{Sb}_2(\text{S,Se})_3$ thin-film solar cells with the substrate configuration of SLG/Mo/ $\text{Sb}_2(\text{S,Se})_3$ /CdS/ITO/Ag. The champion device achieved 4.05% efficiency with a V_{OC} of 463 mV, a J_{SC} of 21.43 mA/cm^2 , and an FF of 41.10%. This study provided an effective post-selenization strategy for improving the quality of the $\text{Sb}_2(\text{S,Se})_3$ film, thereby indicating a potential approach to the fabrication of high-efficiency $\text{Sb}_2(\text{S,Se})_3$ solar cells.

Experimental detail

Preparation of $\text{Sb}_2(\text{S,Se})_3$ thin films.

Prior to depositions, soda-lime glass (SLG) was ultrasonically cleaned in detergent, deionized water, isopropanol, and ethanol for 20 min each and dried in the oven for 10 min. Then a Mo layer with a thickness of approximately 1 μm was sputtered on it via magnetron sputtering with two different working pressures. Before sputtering, the SLG was heated up to 200 $^{\circ}\text{C}$. Then, the first Mo layer was sputtered under 1.5 Pa for 15 min, and the DC power was fixed at 100 W. The second Mo layer was sputtered under 0.5 Pa, and the DC power was fixed at 250 W. After that, the substrates were treated with plasma for 10 min to remove the organic residue from the surface. High purity argon gas (>99.999%) was used as the working gas, and the power was fixed at 100 W. The schematic of the preparation process of the $\text{Sb}_2(\text{S,Se})_3$ thin-film solar cell is provided in **Fig. 1**. As shown in **Fig. 1a**, $\text{Sb}_2(\text{S,Se})_3$ light absorber layer was fabricated by hydrothermal synthesis. The precursor solution was prepared by dissolving 0.267 g of $\text{K}_2\text{Sb}_2(\text{C}_4\text{H}_2\text{O}_6)_2 \cdot 3\text{H}_2\text{O}$, 0.794 g of $\text{Na}_2\text{S}_2\text{O}_3 \cdot 5\text{H}_2\text{O}$, and 0.025 g of $\text{SeC}(\text{NH}_2)_2$ in 40 mL DI water. In a typical process, this mixture was stirred at room temperature for a while until a uniform yellow solution was formed and then poured into the Teflon container. The as-prepared Mo substrate was transferred into a Teflon container and tilted against the wall at a suitable angle. To control the grains size, a hydrothermal reaction was carried out at different temperatures from 125 $^{\circ}\text{C}$ to 145 $^{\circ}\text{C}$, with an interval of 10 $^{\circ}\text{C}$. Besides, for the purpose of controlling the absorber layer thickness, the holding time was changed from 2.5 h to 5.5 h with an interval of 1 h. After that,

samples were taken out, washed with DI water and ethanol, and blow-dried with compressed nitrogen. **Fig. 1b** illustrates that the as-deposited film was selenized in a tube furnace at different temperatures from 390 °C to 440 °C with 0.4 g high-purity Se powder. The chambers were evacuated using a mechanical pump, and high purity argon gas (>99.999%) was introduced to clarify the chambers exhaustively before selenization. Sufficient Se pressure was provided with a high working pressure of 5×10^4 Pa to passivate the Se vacancy and obtain a suitable composition.

Fabrication of $\text{Sb}_2(\text{S},\text{Se})_3$ thin-film solar cells.

After deposition and selenization, the CdS thin film was prepared through the chemical bath deposition method in **Fig. 1c**. Then, the as-deposited CdS thin film was rinsed with DI water and ethanol and dried with nitrogen gas subsequently. As shown in **Fig. 1d**, an ITO window layer was deposited by magnetron sputtering. The ITO window layer was deposited via 120 W RF power, and the deposition time was fixed at 25 min. The thickness of the ITO layer was about 400 nm. Ultimately, silver grids were evaporated on the surface of the obtained Mo/ $\text{Sb}_2(\text{S},\text{Se})_3$ /CdS/ITO stacked layer by the thermal evaporation method. Finally, the $\text{Sb}_2(\text{S},\text{Se})_3$ solar cells were fabricated with a designated area of approximately 0.16 cm² in **Fig. 1e**, and the active area was 0.14 cm².

Characterizations.,

A field-emission scanning electron microscope (SEM, Zeiss SUPRA 55) with an attached energy-dispersive X-ray (EDX) detector (BRUKER QUANTX 200) was used to measure the film morphologies, the chemical compositions, and elemental distribution. The crystal structure of the samples was characterized by an Ultima-iv X-

ray diffractometer with Cu K α as the radiation source under the operation conditions of 40 kV and 40 mA from 10° to 60°. Raman spectroscopy was performed at room temperature using a Raman spectrometer (InVia, Renishaw Inc., UK) equipped with a green laser (532 nm). The photo-electro-chemical (PEC) properties of the thin films were characterized by using a CHI660e electrochemical workstation with a conventional three-electrode configuration. Ag/AgCl in saturated KCl was the reference electrode, Pt-wire was the counter electrode, and the Sb₂(S,Se)₃ photocathode was the working electrode. It was performed under 100 mW/cm² AM 1.5G simulated sunlight illumination in 0.5 M H₂SO₄ electrolyte. The current density–voltage (J–V) curves of the Sb₂(S,Se)₃ devices were measured using a multimeter (Keithley, 2400 Series) under 100 mW/cm² AM 1.5 G light illumination at room temperature, which was calibrated by using a standard Si reference cell. The external quantum efficiency (EQE) spectra were obtained on a solar cell quantum efficiency measurement system (Zolix SCS101 system) and a Keithley 2400 source meter. The capacitance-voltage (CV) and drive-level capacitance profiling (DLCP) were measured using a parameter analyzer (Keithley, 4200A-SCS) with a cryogenic platform (JANIS). The CV profiling measurement was performed at 30 mV, with a 50 kHz AC excitation source at a DC bias from 0 V to –0.25 V at room temperature. The DLCP measurements were performed with an AC amplitude from 20 mV to 140 mV and a DC bias voltage from –0.2 V to 0.2 V at a frequency of 50 kHz. The admittance spectroscopy (AS) measurement (Victor, Digital LCR meter) was carried out within the frequency range of 100–1 MHz at a temperature range of 180–330 K (Lake Shore, 325 cryogenic

temperature controller). The bandgap structure of the $\text{Sb}_2(\text{S,Se})_3$ thin film was characterized by ultraviolet photoelectron spectroscopy (UPS; Thermo Fisher, USA), and a He (I) discharge lamp (21.22 eV) was used as the UV light source. Work function (W_f) and low binding energy tail threshold that refer to the energy difference between the valence band maximum and the Fermi level of the semiconductors were obtained. The work function (W_f) was calculated by subtracting the binding energies of the secondary electron cutoffs (E_{cutoff}) from the excitation light energy ($h\nu$, 21.2 eV).

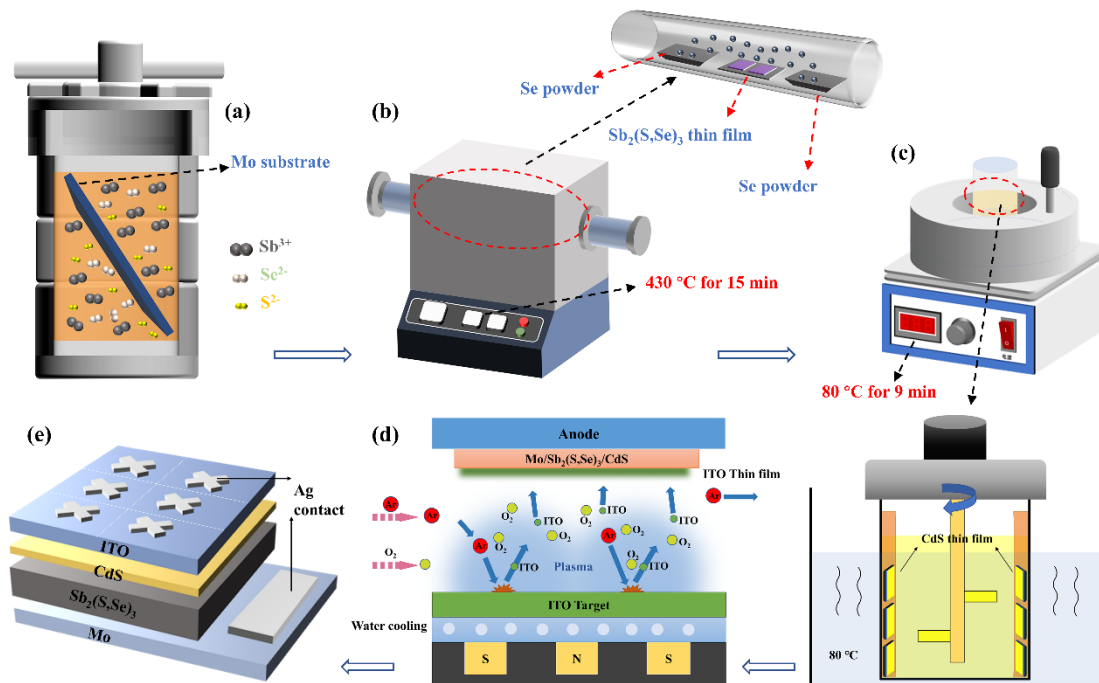


Fig. 1. Schematic diagram showing the complete fabrication process of $\text{Sb}_2(\text{S,Se})_3$ solar cell device. (a) hydrothermal process for $\text{Sb}_2(\text{S,Se})_3$ thin film. (b) Post-selenization heat treatment of $\text{Sb}_2(\text{S,Se})_3$. (c) CdS buffer layer deposited via chemical bath deposition (CBD) method. (d) ITO layer deposited by magnetron sputtering. (e) Schematic configuration of the final $\text{Sb}_2(\text{S,Se})_3$ device.

Result and discussion

Effect of selenization treatment on the performance of $\text{Sb}_2(\text{S,Se})_3$ thin films

To enable the film deposition on the Mo structure, we applied a plasma etcher to remove the organic residue from the surface. I–V characteristics of $\text{Sb}_2(\text{S,Se})_3$ devices based on Mo structure with or without plasma treatment, as depicted in **Figure S1**. Notably, a decent surface is beneficial for film growth. After plasma treatment, the conductivity was enhanced from 0.0727 S m^{-1} to 0.268 S m^{-1} . This improved electrical property is expected to enhance the photovoltaic performance of solar devices. Furthermore, to investigate the relationship between the deposition parameters and the quality of the absorber, a series of $\text{Sb}_2(\text{S,Se})_3$ thin film deposition experiments was carefully designed. **Fig. 1a-c** shows that as measured by SEM, when the holding time was fixed at 2.5 h, and the temperature changed from $125 \text{ }^\circ\text{C}$ to $145 \text{ }^\circ\text{C}$ with an interval of $10 \text{ }^\circ\text{C}$, the grain size of the $\text{Sb}_2(\text{S,Se})_3$ absorber first increased and then became nanoarray with increasing temperature. This funding was likely due to the fact that high deposition temperature may change the nucleation and crystal growth process.²⁹ When the temperature was fixed at $135 \text{ }^\circ\text{C}$, and the holding time was increased from 2.5 h to 5.5 h, the thickness of the $\text{Sb}_2(\text{S,Se})_3$ absorber increased with increasing holding time, as seen in **Figure S2**. This experiment aimed to optimize the thickness to fabricate enough thickness of $\text{Sb}_2(\text{S,Se})_3$ absorber layers and to absorb enough light. Finally, the best deposition parameters (holding time and deposited temperature) were fixed at 5.5 h and $135 \text{ }^\circ\text{C}$, respectively. The grain size was too small to efficiently transport the electricity. As shown in **Figure S3**, the XRD pattern revealed that the as-deposited $\text{Sb}_2(\text{S,Se})_3$ thin

film was an amorphous thin film. Therefore, to improve the crystallinity of thin films and the carrier transport rate, further post-treatment was necessary for $\text{Sb}_2(\text{S,Se})_3$ thin films.

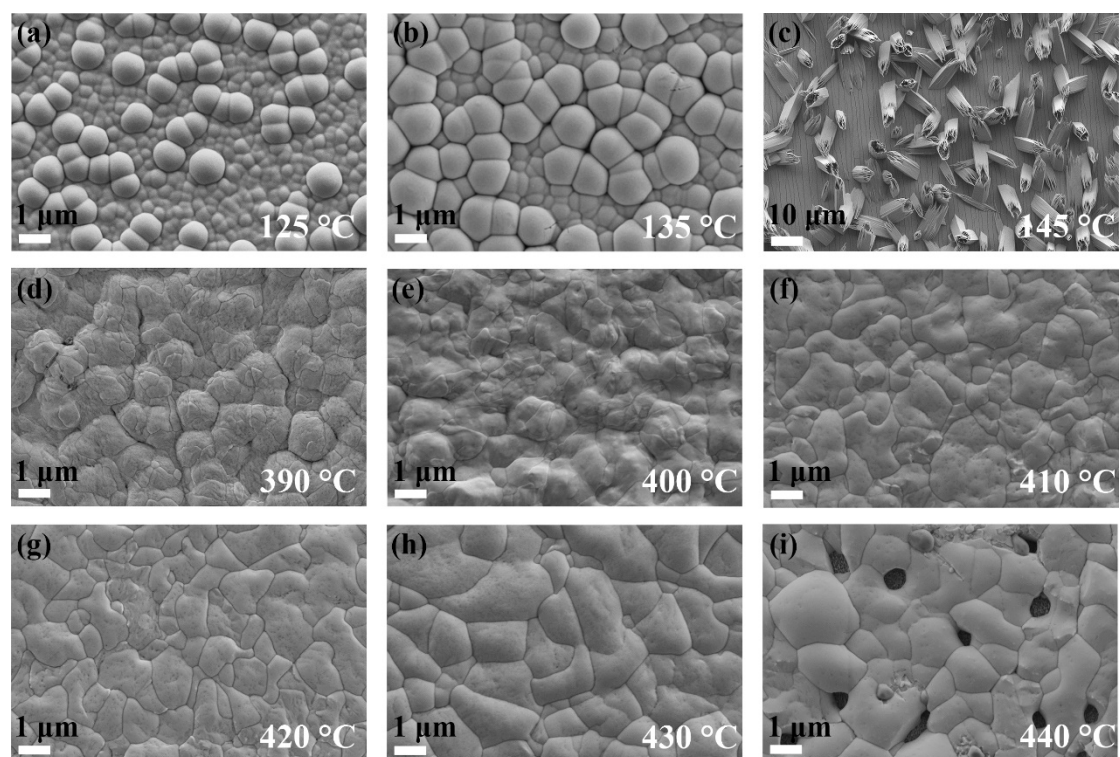


Fig. 2. Plane SEM images of $\text{Sb}_2(\text{S,Se})_3$ precursor thin film deposited by hydrothermal for (a) 125 °C, (b) 135 °C and (c) 145 °C, respectively. And Plane SEM images of $\text{Sb}_2(\text{S,Se})_3$ thin film selenized at (d) 390 °C, (e) 400 °C, (f) 410 °C, (g) 420 °C, (h) 430 °C and (i) 440 °C.

A smooth and uniform surface is a necessary condition in thin-film solar cells for high-performance devices.³⁰ Herein, a post-selenization treatment was introduced to modify the surface of the $\text{Sb}_2(\text{S,Se})_3$ thin films. To establish the relation of selenization parameters for modifying the thin film morphology, a series of experiments was carried out to study the relationship between the selenization parameters and the quality and

chemical composition of $\text{Sb}_2(\text{S,Se})_3$ thin films on Mo substrate. The top-view SEM images are presented in **Fig. 2d-i**. When the selenization time was fixed at 25 min at a selenization temperature of 390 °C, the thin film was composed of tiny grains. The particles grew together under a post-selenization. For the thin films selenized at 400 °C, 410 °C, and 420 °C, the higher the increase in temperature was, the more compact and uniform the coverage of the surface was. This phenomenon can be explained by the regrowth of the thin film under the selenium atmosphere. Notably, much larger grains with sizes over 1 μm can be observed on the film surface when the selenization process was conducted at 430 °C, and they showed the features of compactness and homogeneity. Further improving the temperature led to emerging decomposition, and distinct micro-voids were obtained at a high temperature of 440 °C, as depicted in **Fig. 2i**. This situation can be attributed to Se re-evaporation from $\text{Sb}_2(\text{S,Se})_3$ or film decomposition under high temperature.²⁸ The chemical composition results of the $\text{Sb}_2(\text{S,Se})_3$ thin films analyzed by energy-dispersive X-ray spectroscopy (EDS) are summarized in **Table 1**. Sulfur evaporates more easily at high temperature compared with selenium, because the saturated vapor pressure of sulfur is higher than that of selenium.³¹ With increasing temperature, a large amount of selenium replaced the sulfur, because sulfur reevaporated from the thin film.³² However, for the thin film selenized at 440 °C, the atomic percentage of antimony decreased, suggesting partial decomposition of the thin films due to excessive temperature, which is consistent with the SEM result (**Fig. 2i**).

Table 1 Chemical composition of the $\text{Sb}_2(\text{S},\text{Se})_3$ thin films deposited at different selenization temperatures.

Sample	Sb (%)	S (%)	Se (%)
390 °C	40.5	22.37	37.13
400 °C	39.26	19.51	41.23
410 °C	38.72	16.32	44.96
420 °C	38.09	14.82	47.09
430 °C	38.42	9.27	52.31
440 °C	35.87	9.21	54.92

To determine the reason for the improved quality after selenization treatment, a series of experiments in terms of thin-film characterization was designed. As shown in **Fig. 3a**, the Raman spectra of the $\text{Sb}_2(\text{S},\text{Se})_3$ thin-film exhibited two major peaks at 191 and 210 cm^{-1} , which could be ascribed to the Sb-Se vibration and heteropolar Sb-Se stretching vibration in Se chains, respectively.³³ The absence of other observable characteristic peaks, such as Sb-S bond vibration (282 and 310 cm^{-1})³⁴, which could be due to the complete selenization of the $\text{Sb}_2(\text{S},\text{Se})_3$ thin-films surface, was noted. Only a little sulfur remained with a strong chemical bond at the back interface. Moreover, as the selenization temperature was rising, the dominant peak at 191 cm^{-1} was sharper and the peak at 210 cm^{-1} disappeared.²⁷ As the selenization temperature increased, the crystallinity and purity of the samples were enhanced. To further study the effect of selenization treatment on the crystallization property of $\text{Sb}_2(\text{S},\text{Se})_3$ film, X-ray

diffraction (XRD) patterns were recorded for $\text{Sb}_2(\text{S,Se})_3$ films at different temperatures. Compared with the standard pattern of Sb_2S_3 (JCPDS Card No. 42-1393), X-ray diffraction peaks of $\text{Sb}_2(\text{S,Se})_3$ shifted to the lower 2-Theta angles without any detectable impurities or secondary phase after selenization treatment. The enlarged lattice spacing issues could be explained by the big atom Se replacing the small atom S, which led to the expansion of the unit cell volume during the selenization treatment.³⁵ As the temperature increased from 390 °C to 430 °C, an obvious increase in peaks intensities was observed, which suggested the increasing crystallinity of the $\text{Sb}_2(\text{S,Se})_3$ thin films upon selenization treatment. Until the temperature reached 440 °C, the intensities of the peaks tended to decrease, because high temperature led to film decomposition, which was consistent with the SEM results. Compared with the hydrothermal deposition on the FTO structure, the XRD pattern of $\text{Sb}_2(\text{S,Se})_3$ thin films deposited on the Mo structure showed that the growth direction was dominated by the [hk1] direction, which was beneficial for carrier transport along the [hk1] direction. The texture coefficient (TC) was further introduced to investigate the thin film growth orientation.^{10, 36} It could be calculated according to the following equation³⁷:

$$TC(hkl) = \frac{I(hkl)}{I_0(hkl)} / \left(\frac{1}{N} \sum_{i=1}^N \frac{I(h_i k_i l_i)}{I_0(h_i k_i l_i)} \right) \quad (1)$$

where $I(hkl)$ is the measured diffraction intensity of the (hkl) plane, $I_0(hkl)$ is the reported diffraction intensity in the standard PDF card, and N is the number of peaks adopted in the calculation. **Fig. 3d** shows that the reduction of the TC of the $(hk0)$ planes and the increase of the TC of the (hkl) planes when the temperature increased from

390 °C to 440 °C. Notably, when the temperature was fixed at 430 °C, the smallest TC of (*hk*0) planes and the highest TC of (*hkl*) planes can be observed. According to the previous research, the high TC of a diffraction peak demonstrated the preferred orientation and an increase in packing density along this designated direction.³⁸

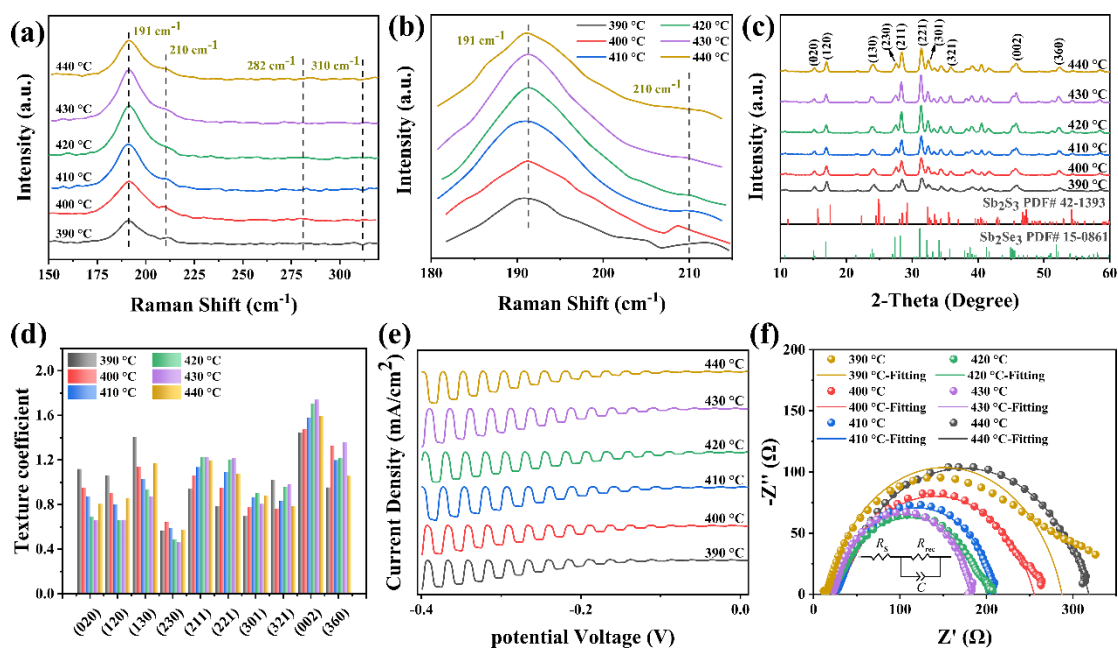


Fig. 3. (a) Raman spectra of the $\text{Sb}_2(\text{S,Se})_3$ thin film under different selenization conditions. (b) enlarged region of the Raman spectra from 180 to 215 cm^{-1} . (c) XRD patterns, (d) texture coefficients, (e) Current Density-potential Voltage, and (f) electrochemical impedance spectroscopies of the $\text{Sb}_2(\text{S,Se})_3$ thin film under different selenization conditions, the inset is the equivalent circuit model.

To further investigate the function of selenization treatment, the photoconductive characteristics of the $\text{Sb}_2(\text{S,Se})_3$ -based thin films were measured via the classical 3-electrode photoelectrochemical (PEC) measurements. These electrodes were simultaneously immersed into the electrolyte (0.5 M H_2SO_4 solution) and underwent

AM 1.5G light illumination. The chopped light can be obtained by a mechanical chopper at a frequency of 5 Hz. The chopped light determined current density versus voltage curves as depicted in **Fig. 3e**. The $\text{Sb}_2(\text{S,Se})_3$ -based thin films under different selenization temperatures were used as the working electrode. All the $\text{Sb}_2(\text{S,Se})_3$ -based thin films can produce a photocurrent density at negative bias, even with no photocurrent density at positive bias, which indicated its P-type conductive character.³⁹ The photocurrent density at -0.4 V were -3.338 , -3.375 , -3.677 , -3.840 , -4.414 , and -3.467 mA/cm^2 , respectively. Interestingly, the trend of photocurrent density variation was consistent with a previous experiment's results, further confirming the enhancement of crystallinity and quality of the $\text{Sb}_2(\text{S,Se})_3$ thin films. The impedance of electron transport of $\text{Sb}_2(\text{S,Se})_3$ thin films with selenization treatment was diagnosed as shown in **Fig. 3f**. The inset of **Fig. 3f** exhibits the equivalent electronic circuit that was used to fit the impedance spectra, in which R_s was the series resistance, and the R_{rec} was the recombination resistance.⁴⁰ The impedance of $\text{Sb}_2(\text{S,Se})_3$ thin films decreased first as the selenization temperature increased because post-selenization treatment led to the enhancement of crystallinity. Further annealing at 440 °C led to thin-film decomposition. The crystallinity of the film increased with the selenization temperature, which was undoubtedly beneficial for carrier transport. However, the film decomposed at high temperature led to chemical composition shifts. According to **Fig. 3f**, due to the decomposition of $\text{Sb}_2(\text{S,Se})_3$ film, the electron transport impedance of $\text{Sb}_2(\text{S,Se})_3$ film increased to a certain extent.⁴¹

Overall, by carefully optimizing the selenization treatment parameters, we found that

selenization temperature plays an important role in obtaining high-quality $\text{Sb}_2(\text{S},\text{Se})_3$ film. A suitable temperature would enhance crystallinity and improve the quality of the films, whereas improper temperature would lead to decomposition of the $\text{Sb}_2(\text{S},\text{Se})_3$ film, thereby hindering the carrier transport. It was not suitable for device fabrication. Finally, the best parameters of selenization were fixed at 430 °C and 20 min for the temperature and holding time, respectively.

Effect of selenization treatment on the performance of $\text{Sb}_2(\text{S},\text{Se})_3$ solar cells

To visualize the validity of this selenization treatment, $\text{Sb}_2(\text{S},\text{Se})_3$ solar cells were fabricated using the optimized films with a device configuration of Mo/ $\text{Sb}_2(\text{S},\text{Se})_3$ /CdS/ITO/Ag. For clarity of description, the samples with different selenization temperatures were marked as SS1, SS2, and SS3 for 420 °C, 430 °C, and 440 °C, respectively. J-V curves shown in **Fig. 4a** easily demonstrated that the hysteresis effect was negligible because of the nearly overlapping J-V curves in the forward and reverse scan directions. The SS2 exhibited the best performance among these devices, and the detailed PV parameters are provided in **Table 2**. The best device derived from the optimized $\text{Sb}_2(\text{S},\text{Se})_3$ thin film exhibited a conversion efficiency of 4.05% with a V_{OC} of 463 mV, a J_{SC} of 21.43 mA/cm², and an FF of 41.10%. Notably, the improvement of the efficiency after optimization was attributed to the synergetic improvement of V_{OC} , J_{SC} , and FF, which demonstrated that the suitable selenization treatment may improve the crystalline and the carrier transport quality of $\text{Sb}_2(\text{S},\text{Se})_3$ absorber in addition to the quality of $\text{Sb}_2(\text{S},\text{Se})_3$ /CdS interface. Moreover, the improved FF from 38.80% to 41.10% indicated that the improved crystallinity and the decreased

impedance of electron transport may optimize the interface or bulk defects in the $\text{Sb}_2(\text{S,Se})_3$ solar cell. This will be discussed in detail in the following section. Additionally, the statistics of performance parameters from the three devices demonstrated the good repeatability of fabrication, as observed in **Figure S4**. However, the SS3 device exhibited the worst performance, which can be explained by the fact that the decomposition of the $\text{Sb}_2(\text{S,Se})_3$ film led to the increased impedance of electron transport, as shown in **Fig. 3**. This is harmful for fabrication of the solar cell. Overall, compared with the FTO-structure-based device, the best efficiency of the Mo-structure-based device can potentially be obtained through post-selenization treatment.

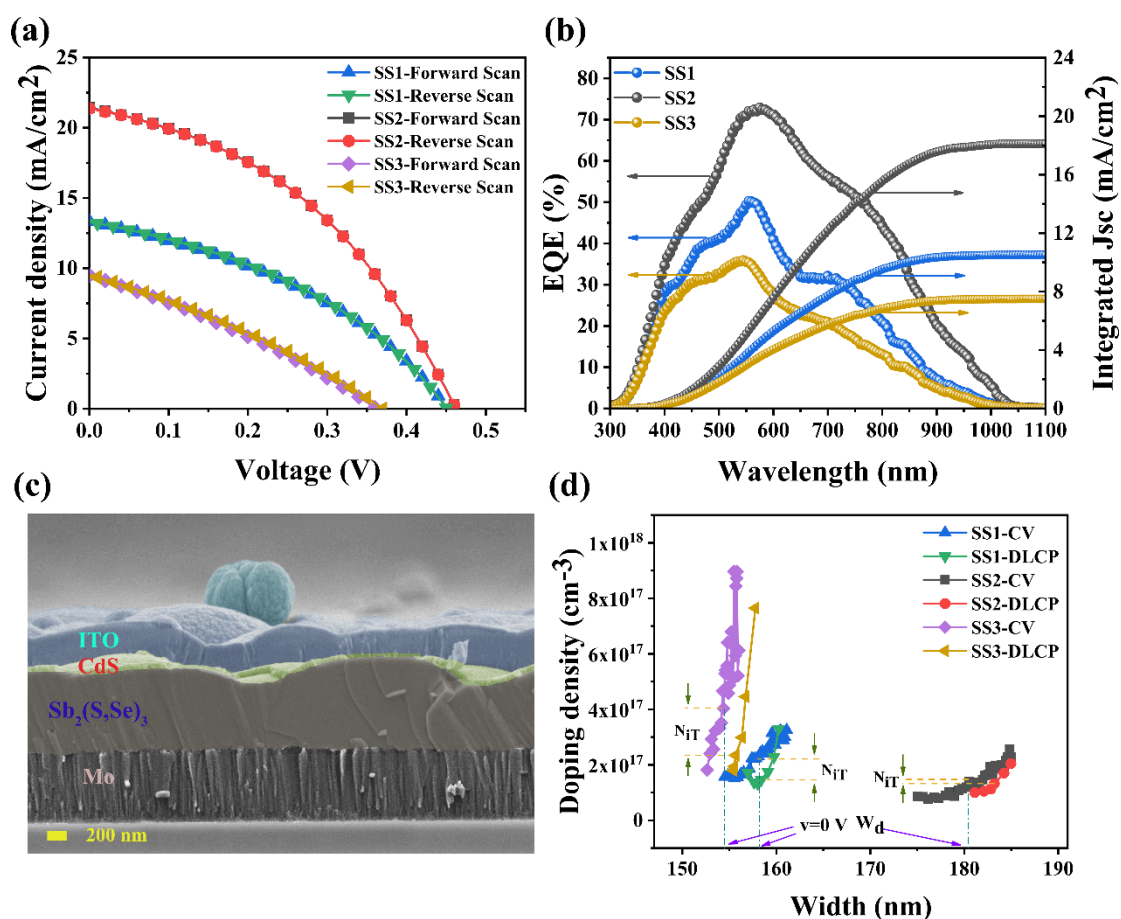


Fig. 4. Device performance characterizations of the $\text{Sb}_2(\text{S,Se})_3$ solar cells. (a) J-V curves with different scanning directions and (b) EQE spectrums and the integrated J_{sc}

of the SS1, SS2, and SS3 devices. (c) Cross-sectional SEM image of the SS2 device.

(d) C-V profiling and DLCP profiling of the SS1, SS2, and SS3 devices.

Table 2 Device parameters of the $\text{Sb}_2(\text{S,Se})_3$ solar cell deposited at different selenization temperatures.

Sample	V_{OC} [V]	J_{SC} [mA/cm ²]	FF [%]	PCE [%]	R_S [Ω]	R_{SH} [Ω]	A	J_0 [mA/cm ²]	E_g (eV)	$V_{OC, def}$ [V] $E_g/q - V_{OC}$
SS1	0.452	13.34	38.80	2.28	95.6	639.1	2.09	1.30×10^{-4}	1.51	1.058
SS2	0.463	21.43	41.10	4.05	66.9	630.7	1.87	2.88×10^{-4}	1.46	0.997
SS3	0.362	9.48	30.13	1.03	189.4	423.1	2.91	1.60×10^{-2}	1.42	1.058

To further evaluate the quality of the optimized $\text{Sb}_2(\text{S,Se})_3$ device, the external quantum efficiency (EQE) spectra of the above devices are presented in **Fig. 4b**. The response of the $\text{Sb}_2(\text{S,Se})_3$ solar cell was in the range of 300 – 1100 nm. There was no doubt that the EQE loss in the range below 500 nm resulted from the parasitic absorption caused by the CdS, which was consistent with previously reported $\text{Sb}_2(\text{S,Se})_3$ solar cells.⁴² Similar absorption was observed in the short wavelength range, thereby demonstrating the same property of N-type layers. Observably, the EQE result of the SS2 device was better than those of the others. The EQE response of the SS2 device reached over 70% in the 550 – 650 nm wavelength region. The increased EQE value in the range of 300 – 500 nm can be attributed to the improved quality PN junction. The enhancement in the range of 550 – 1000 nm was presumably due to the promoted crystallinity of the

absorber and the quality of the back interface. For the other devices, the obvious decrease in this region was probably due to a slower extraction and more serious recombination of minority carriers in the bulk of the absorber film. By integrating the EQE spectra, the J_{SC} values for the three devices were 10.51, 18.12, and 7.49 mA/cm², which agreed well with the J_{SC} from the J-V curve. Moreover, the band gaps of all absorbers were calculated by extrapolation of $(d(\ln(1-EQE)/dE))$ versus E plots and were estimated to be around 1.51, 1.46, and 1.42 eV for SS1, SS2, and SS3 devices, respectively (**Figure S5**). After the selenization process, the band gap decreased with increasing temperature because many selenium atoms replaced the sulfur atom. With a smaller bandgap, the broader absorption allowed the absorption of more photons.³¹ So, the increase of J_{SC} can be explained by the improvement of the EQE. The cross-sectional SEM images for SS1, SS2, and SS3 devices are presented in **Figs. 4c** and **S6**. The SEM image of the SS2 device presented a compact absorber and decent back interface, which was beneficial for device fabrication. However, many small holes were present at the interface between the $Sb_2(S,Se)_3$ absorber and Mo layer, which aggravated interfacial recombination and seriously affected the extraction and transport of carriers,⁴³ as shown in **Figure S6a**. Additionally, as the yellow dotted box showed in **Figure S6b**, the absorber layer decomposed and the CdS buffer layer was in direct contact with the Mo structure, thereby causing the battery to have a short circuit and affecting device efficiency.

The junction-dependent electrical behaviors of the three devices were systematically estimated by treating the dark J-V characteristic curves (FigureS7). The values of

ideality factor (A), the reverse saturated current (J_0), and the shunt conductance (G) and resistance (R) are presented in **Table 2**. These can be calculated by using the single exponential diode equation¹⁸:

$$J = J_0 \exp \left[\frac{q}{AkT} (V - JR) \right] + GV - J_L \quad (2)$$

Notably, compared with SS1 device, the A value of SS2 device decreased from 2.09 to 1.87, and the J_0 value was reduced from 1.30×10^{-4} mA/cm² to 2.88×10^{-4} mA/cm², thereby implying that the heterojunction quality of SS2 device became better and indicating the optimized interface recombination. The A value of SS3 device reached 2.91, and the J_0 of 1.6×10^{-2} mA/cm² was poor, which indicated that the most severe interface recombination resulted in the lowest efficiency. According to the above experimental results, we preliminarily assumed that the enhancement of device efficiency by selenization treatment was attributed to the fewer defects at the heterojunction interface. To further attest to this assumption, the capacitance–voltage (C–V) and deep-level capacitance profiling (DLCP) measurements were introduced to characterize the defect density at the Sb₂(S,Se)₃/CdS interface and the quality of the Sb₂(S,Se)₃/CdS heterojunction. According to literature, the carrier doping density obtained from CV profiling mainly represented responses from free carriers, bulk defects, and interfacial defects, whereas that obtained from DLCP profiling only reflected responses from free carriers and bulk defects.¹⁸ So, the discrepancy in the doping density between CV and DLCP resulted indirectly reflects the information of interfacial defects. The plots of N_{CV} and N_{DLCP} against the profiling depth x can be calculated by the following equation⁴⁴:

$$N_{CV} = \frac{-2\varepsilon_{r,n}N_D}{\left(\frac{d\left(\frac{1}{C^2}\right)}{dV}\right)qA^2\varepsilon_0\varepsilon_{r,n}\varepsilon_{r,p}N_D + 2\varepsilon_{r,p}} \quad (3)$$

$$N_{DLCP} = -\frac{C_0^3}{2q\varepsilon_0\varepsilon_{r,p}A^2C_1}, \quad (4)$$

$$x = \frac{\varepsilon_0\varepsilon_{r,p}A}{C_0} \quad (5)$$

where N_D is the doping density of CdS; A is the device area; $\varepsilon_{r,n}$ and $\varepsilon_{r,p}$ are the relative permittivity of CdS and $\text{Sb}_2(\text{S,Se})_3$, respectively; and C_0 and C_1 are two quadratic fitting parameters derived from the DLCP curves. As shown in **Fig. 4d**, the depletion layer width (W_d) can be deduced from the CV curves. There were 158, 181, and 154 nm for SS1, SS2, and SS3 devices, respectively. Usually, a larger depletion region was beneficial for enhancing the separation and extraction of carriers, thus leading to the increase of J_{SC} .⁴¹ The doping density values obtained from CV (N_{CV}) curves and DLCP (N_{DLCP}) of SS1 device were 2.22×10^{17} and $1.71 \times 10^{17} \text{ cm}^{-3}$, respectively, the disparity between N_{CV} and N_{DLCP} was $5.1 \times 10^{16} \text{ cm}^{-3}$. Apparently, a smaller difference in doping density profiles was found between CV and DLCP for the SS2 device than that for the SS1 device. The N_{CV} and N_{DLCP} doping densities slightly decreased to 1.19×10^{17} and $1.00 \times 10^{17} \text{ cm}^{-3}$, respectively. Hence, the interface defect density of the SS2 device was $1.90 \times 10^{16} \text{ cm}^{-3}$, which was lower than that of the SS1 device. The interface defects density decreased, thereby indicating that carriers are not easily captured as recombination centers and are more easily transported at the interface; thus, the collection of carriers improved, and performance of the device increased.⁴⁵ Nevertheless, the interface defect density of the SS3 device reached $2.22 \times 10^{17} \text{ cm}^{-3}$,

which was an order of magnitude higher than those of other devices. This finding demonstrated that there were severe recombination losses at the interface, which led to poorer device performance. This result was in accordance with our assumption.

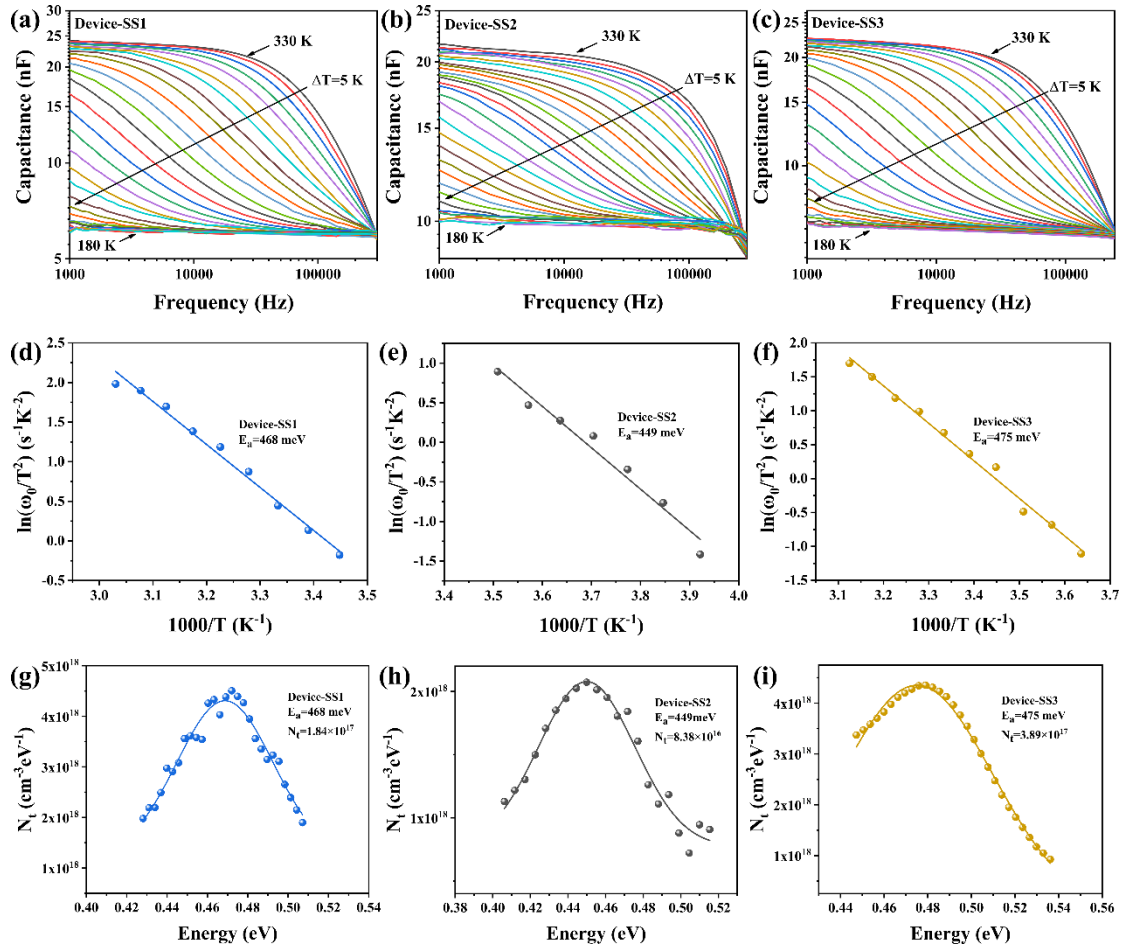


Fig. 5. (a-c) Capacitance–frequency–temperature (C–f–T) spectra, (d-f) the Arrhenius plots of ω_0/T^2 versus $1000/T$ for a defect (the defect activation energies (E_a) were calculated for each defect and are shown inside the figure) and (g-i) defect densities of the defect derived from the admittance spectra of SS1, SS2, and SS3 devices, respectively.

To obtain the relative quantitative information about the carriers and the deep level defect concentrations, the admittance spectroscopy (AS) measurements were applied.

Fig. 5a-c demonstrates the temperature-dependent capacitance-frequency (C-f-T) spectra obtained over the temperature range of 180 K to 330 K at steps of 5 K of the devices. The spectra were measured in the dark from 10^2 Hz to 10^6 Hz, with an AC voltage of 25 mV and DC bias of zero during the measurement. According to previous literature, the capacitance response at low frequency represents the deep level traps and free carriers, whereas the capacitance at high frequency represents the response of the free carrier density.⁴⁶ **In Fig. 5b**, the capacitance of the SS2 device demonstrated a smaller change as a function of frequencies and temperatures when compared with the other two devices, indicating the lower defect density for the device. Moreover, as capacitance of data converges at low temperature and high frequency, it was probably determined by the geometric capacitance of the devices due to carrier freeze-out.⁴⁷⁻⁴⁸

Fig. 5d-f shows the Arrhenius plot for the inflection points in the three admittance spectra, respectively. The inflection point frequency ω_0 of each CF curve was derived from the angular frequency point ω at the maximum of the $\omega dC/d\omega$ plot. The fitting of the Arrhenius plot was according to the following equation¹⁴:

$$\omega_0 = 2\pi\nu_0 T^2 \exp\left(\frac{-E_a}{kT}\right) \quad (6)$$

where ν_0 is the attempt-to-escape frequency; ω_0 is the inflection point frequency; k is the Boltzmann constant; and E_a is the defect activation energy, the energetic depth of the defect relative to the corresponding band edge. The E_a can be extracted from the plot of $\ln(\omega/T) \sim 1000/T$. The E_a was around 468, 449, and 475 meV for the SS1, SS2, and SS3 devices, respectively. According to a previous study on first-principle calculation, there were mainly two defects in $Sb_2(S,Se)_3$; one can be ascribed to

selenium vacancy (V_{se}), and the other can be ascribed to antimony antisite (Sb_{se}). It was logical that both defects were present in the device.¹⁴ Considering that only one defect level was detected in the AS measurement, we tentatively attributed V_{se} and Sb_{se} to the dominant defect of our devices. A general decrease of activation energy with optimizing the selenization treatment parameter was clearly visible in the AS data. The change of defect activation energy in three devices likely corresponded to the shifts of the valence band maximum that resulted from the different selenization temperatures in the $Sb_2(S,Se)_3$ absorber. The S p level was lower than Se. Thus, the VBM of the sulfides was lower than that of the selenides.³¹ With increasing selenization temperature, the valence band moved up, potentially yielding defects with lower ionization energies, which was beneficial for reducing the recombination losses. High activation energies tended to act as more effective recombination centers, thus hindering the carrier transport.⁴⁹ The activation energy of the SS1 device was higher than that of the SS2 device, demonstrating the more serious recombination loss in the SS1 device. This observation was also correlated with EQE (**Fig. 4b**). Moreover, the SS3 device exhibited a much lower EQE response, which can possibly be explained by significant recombination losses due to increased defect activity, resulting in a more severe decline in device performance.

To further evaluate the defects, the defect density values of the three devices were Gaussian fitted using the Kimerling model based on the following equation⁵⁰:

$$E(\omega) = kT \ln \left(\frac{2\pi\nu_0 T^2}{\omega} \right) \quad (7)$$

$$N_t(E(\omega)) = -\frac{V_d}{q\omega} \frac{dC}{d\omega} \frac{\omega}{kT} \quad (8)$$

where E is the energetic distance between the defect energy level and the VBM or CBM, V_d is the built-in voltage of the heterojunction (as depicted in **Figure S8**), and ω is the angular frequency. The fitted defect density plots of the three devices are shown in **Fig. 5g-i**, which represented the situation in a small range. Notably, the efficiency of the device was not only positively associated with the defect density, but also the activation energy of the defect was. The integrated defect densities of the three devices are 1.84×10^{17} , 8.38×10^{16} , and $3.89 \times 10^{17} \text{ cm}^{-3}$, respectively. With increasing the defect density, it was much easier for the defect to act as a recombination center, thus yielding recombination losses both in $\text{Sb}_2(\text{S,Se})_3$ absorber and heterojunction interface and weakening the device performance. The SS2 device presented the lowest defect density, because the $\text{Sb}_2(\text{S,Se})_3$ absorber under an optimized selenization temperature (430 °C) can effectively passivate the defect for the device.

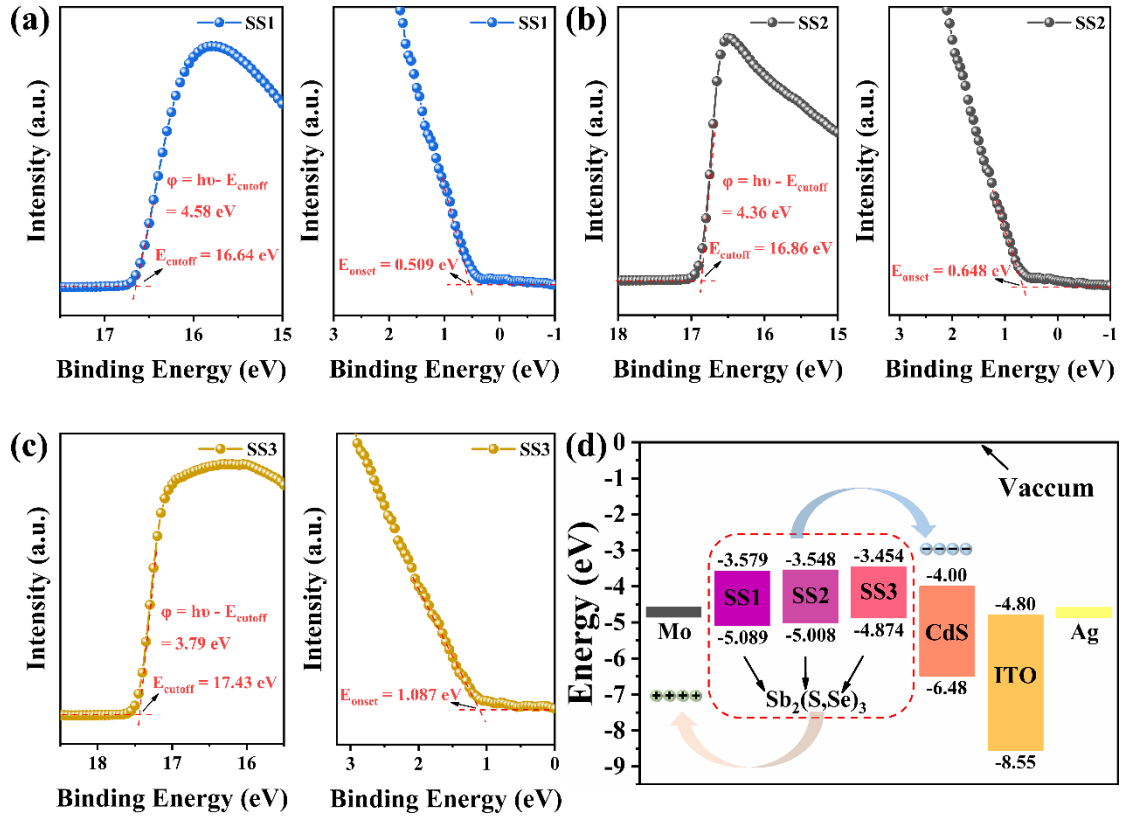


Fig. 6. Secondary electron cut-offs and valence band edge were estimated from the UPS spectra of (a-b) SS1, (c-d) SS2, and (e-f) SS3 thin film, respectively. (g) schematical diagram of the band alignment about SS1, SS2, and SS3 devices.

We analyzed the device performance from the energy level perspective, because the device performance had a strong correlation with the band-gap alignment. The band level of $\text{Sb}_2(\text{S,Se})_3$ film was measured by UPS, as shown in **Fig. 6a-c**. The cutoff edge (E_{cutoff}) values of SS1, SS2, and SS3 devices near the surface were 16.64, 16.86, and 17.43 eV, respectively. The distance from the vacuum level to the Fermi level can be calculated by the following equation⁵¹:

$$\varphi = h\nu - E_{\text{cutoff}} \quad (9)$$

where $h\nu$ is the ultraviolet photoelectron energy of 21.22 eV. The Fermi level were

calculated to be 4.58, 4.36, and 3.79 eV for SS1, SS2, and SS3, respectively. Finally, according to the E_{onset} values, the valence band maximum (VBM) values of the SS1, SS2, and SS3 were estimated to be -5.089, -5.008, and -4.874 eV, respectively. According to **Figure S5**, the bandgap of the SS1, SS2, and SS3 were 1.51, 1.46, and 1.42 eV, respectively. As a result, the conduction band minimum (CBM) values of the SS1, SS2, and SS3 is estimated to be -3.579, -3.548, and -3.454 eV, respectively. In comparison, the Fermi energy of SS2 was upshifted to 4.36 eV, which may likely increase the conductivity of $\text{Sb}_2(\text{S,Se})_3$ film. This can be confirmed by PEC measurement (**Fig. 3e**). The Fermi energy of SS3 was upshifted to 3.787 eV, which was different from the other two device. This may be due to the decomposition of the film at higher selenization temperature. The band alignment diagram of our device is illustrated in **Fig. 6d**; the energy levels of CdS and ITO were obtained from the literature.²⁸ A favorable CBO is regarded to be 0 - 0.3 eV with a spike-like alignment, which can impede the recombination of carriers at the interface and thus improve the quality of the PN junction.^{45, 52} However, all the devices presented the “clifflike” structure and the CBO values of the SS1, SS2, and SS3 are estimated to be 0.421, 0.452, and 0.546 eV. The CBO of the SS3 device was up to 0.546 eV, which was far from the ideal band alignment. Thus, this may be one of the main reasons for the low efficiency of the device. To further improve the device performance, the most important thing to do is to optimize the band alignment. For example, optimizing the back contact, interface modification, and chemical etching may be beneficial for obtaining ideal band alignment.^{42, 45, 53}

Conclusions

$\text{Sb}_2(\text{S,Se})_3$ light absorbing thin films were successfully fabricated via an effective two-step deposition process involving pre-hydrothermal and post-selenization. The $\text{Sb}_2(\text{S,Se})_3$ thin film solar cell with a substrate configuration of SLG/Mo/ $\text{Sb}_2(\text{S,Se})_3$ /CdS/ITO/Ag was constructed, and the mechanism of the post-selenization treatment on crystal growth of $\text{Sb}_2(\text{S,Se})_3$ thin film and the performance of its device were carefully explored. The thin film under 430 °C selenization showed improved crystallinity and larger crystal grains. Meanwhile, the interface defect density can be decreased from $5.1 \times 10^{16} \text{ cm}^{-3}$ to $1.9 \times 10^{16} \text{ cm}^{-3}$, the defect activation energy estimated from the AS can be decreased from 468 meV to 449 meV, and the defect density of absorber bulk can be decreased from $1.84 \times 10^{17} \text{ cm}^{-3}$ to $8.38 \times 10^{16} \text{ cm}^{-3}$. By these abovementioned changes, the defect recombination loss both in interface and bulk can be greatly decreased. The champion device exhibited 4.05% efficiency with a V_{OC} of 463 mV, a J_{SC} of 21.43 mA/cm², and FF of 41.10%. This study demonstrated the great potential of the hydrothermal and post-selenization method in the fabrication of high efficiency $\text{Sb}_2(\text{S,Se})_3$ thin film solar cells based on substrate structure.

Supporting information

Additional SEM images and XRD of precursor film morphology and Electrical behaviors of the samples.

Acknowledgements

This work was supported by National Natural Science Foundation of China (No. 62074102, 62104157 and 62104156), China; Key Project of Department of Education

of Guangdong Province (No. 2018KZDXM059), China; Natural Science Foundation of Guangdong Province (2020A1515010805), China; Science and Technology plan project of Shenzhen (JCYJ20190808153409238 and 20200812000347001), China.

Author Contributions

G.L. supervised the project. G.L. and G.C. conceived the idea and designed the project. G.C. fabricated the devices and conducted the photovoltaic characterizations. R. T. S. C. Z.Z. and H.M. participated in data analysis. Z.X. and P. F helped with the manuscript preparation and analysis. G.C. wrote the paper and all the authors commented on the manuscript.

Conflicts of Interest

There are no conflicts to declare.

Data Availability Statement

The original data in this work is available from the corresponding authors upon reasonable request.

References

- (1) Nakamura, M.; Yamaguchi, K.; Kimoto, Y.; Yasaki, Y.; Kato, T.; Sugimoto, H. Cd-Free Cu(In,Ga)(Se,S)₂ Thin-Film Solar Cell with Record Efficiency of 23.35%. *IEEE J. Photovolt.* **2019**, *9*, 1863-1867.
- (2) Green, M. A.; Dunlop, E. D.; Hohl-Ebinger, J.; Yoshita, M.; Kopidakis, N.; Ho-Baillie, A. W. Y. Solar Cell Efficiency Tables (Version 55). *Prog Photovolt Res Appl.* **2019**, *28*, 3-15.
- (3) Wang, X.; Tang, R.; Jiang, C.; Lian, W.; Ju, H.; Jiang, G.; Li, Z.; Zhu, C.; Chen, T. Manipulating

the Electrical Properties of $\text{Sb}_2(\text{S,Se})_3$ Film for High-Efficiency Solar Cell. *Adv. Energy Mater.* **2020**, *10*, No.2002341.

(4) Qian, C.; Li, J.; Sun, K.; Jiang, C.; Huang, J.; Tang, R.; Green, M.; Hoex, B.; Chen, T.; Hao, X. 9.6%-Efficient All-Inorganic $\text{Sb}_2(\text{S,Se})_3$ Solar Cells with a MnS Hole-Transporting Layer. *J. Mater. Chem. A* **2022**, *10*, 2835-2841.

(5) Li, H.; Lin, L.; Yao, L.; Wu, F.; Wei, D.; Liu, G.; Huang, Z.; Chen, S.; Li, J.; Chen, G. High-Efficiency $\text{Sb}_2(\text{S,Se})_3$ Solar Cells with New Hole Transport Layer-Free Back Architecture via 2D Titanium-Carbide Mxene. *Adv. Funct. Mater.* **2022**, *32*, No.2110335.

(6) Hu, X.; Tao, J.; Wang, R.; Wang, Y.; Pan, Y.; Weng, G.; Luo, X.; Chen, S.; Zhu, Z.; Chu, J.; Akiyama, H. Fabricating over 7%-Efficient $\text{Sb}_2(\text{S,Se})_3$ Thin-Film Solar Cells by Vapor Transport Deposition Using Sb_2Se_3 and Sb_2S_3 Mixed Powders as the Evaporation Source. *J. Power Sources* **2021**, *493*, No.229737.

(7) Tang, R.; Wang, X.; Lian, W.; Huang, J.; Wei, Q.; Huang, M.; Yin, Y.; Jiang, C.; Yang, S.; Xing, G.; Chen, S.; Zhu, C.; Hao, X.; Green, M. A.; Chen, T. Hydrothermal Deposition of Antimony Selenosulfide Thin Films Enables Solar Cells with 10% Efficiency. *Nat. Energy* **2020**, *5*, 587-595.

(8) Lei, H.; Chen, J.; Tan, Z.; Fang, G. Review of Recent Progress in Antimony Chalcogenide-Based Solar Cells: Materials and Devices. *Sol. RRL* **2019**, *3*, No.1900026.

(9) Li, K.; Lu, Y.; Yang, X.; Fu, L.; He, J.; Lin, X.; Zheng, J.; Lu, S.; Chen, C.; Tang, J. Filter-Free Self-Power $\text{CdSe/Sb}_2(\text{S}_{1-x}\text{Se}_x)_3$ Nearinfrared Narrowband Detection and Imaging. *InfoMat* **2021**, *3*, 1145-1153.

(10) Zhou, Y.; Wang, L.; Chen, S.; Qin, S.; Liu, X.; Chen, J.; Xue, D. J.; Luo, M.; Cao, Y.; Cheng, Y.; Sargent, E. H.; Tang, J. Thin-film Sb_2Se_3 Photovoltaics with Oriented One-Dimensional Ribbons and Benign Grain Boundaries. *Nat. Photonics* **2015**, *9*, 409-415.

(11) Wen, X.; Chen, C.; Lu, S.; Li, K.; Kondrotas, R.; Zhao, Y.; Chen, W.; Gao, L.; Wang, C.; Zhang, J.; Niu, G.; Tang, J. Vapor Transport Deposition of Antimony Selenide Thin Film Solar Cells with 7.6% Efficiency. *Nat. Commun* **2018**, *9*, No.2179.

(12) Chen, C.; Bobela, D. C.; Yang, Y.; Lu, S. C.; Zeng, K.; Ge, C.; Yang, B.; Gao, L.; Zhao, Y.; Beard, M. C.; Tang, J. Characterization of Basic Physical Properties of Sb_2Se_3 and its Relevance for Photovoltaics. *Front. Optoelectron* **2017**, *10*, 18-30.

(13) Jin, X.; Fang, Y.; Salim, T.; Feng, M.; Yuan, Z.; Hadke, S.; Sum, T. C.; Wong, L. H. Controllable Solution-Phase Epitaxial Growth of Q1D $\text{Sb}_2(\text{S,Se})_3/\text{CdS}$ Heterojunction Solar Cell with 9.2%

Efficiency. *Adv. Mater.* **2021**, *33*, No.2104346.

(14) Pan, Y.; Hu, X.; Guo, Y.; Pan, X.; Zhao, F.; Weng, G.; Tao, J.; Zhao, C.; Jiang, J.; Chen, S.; Yang, P.; Chu, J. Vapor Transport Deposition of Highly Efficient $\text{Sb}_2(\text{S,Se})_3$ Solar Cells via Controllable Orientation Growth. *Adv. Funct. Mater.* **2021**, *31*, No.2101476.

(15) Wang, W.; Yao, L.; Dong, J.; Wu, L.; Cao, Z.; Hui, L.; Chen, G.; Luo, J.; Zhang, Y. Interface Modification Uncovers the Potential Application of $\text{SnO}_2/\text{TiO}_2$ Double Electron Transport Layer in Efficient Cadmium-Free Sb_2Se_3 Devices. *Adv. Mater. Interfaces* **2022**, *9*, No.2102464.

(16) Yang, B.; Qin, S.; Xue, D. J.; Chen, C.; He, Y. S.; Niu, D.; Huang, H.; Tang, J. In Situ Sulfurization to Generate $\text{Sb}_2(\text{Se}_{1-x}\text{S}_x)_3$ Alloyed Films and Their Application for Photovoltaics. *Prog Photovolt Res Appl.* **2017**, *25*, 113-122.

(17) Zhao, Y.; Wang, S.; Jiang, C.; Li, C.; Xiao, P.; Tang, R.; Gong, J.; Chen, G.; Chen, T.; Li, J.; Xiao, X. Regulating Energy Band Alignment via Alkaline Metal Fluoride Assisted Solution Post-Treatment Enabling $\text{Sb}_2(\text{S,Se})_3$ Solar Cells with 10.7% Efficiency. *Adv. Energy Mater.* **2022**, *12*, No.2103015.

(18) Liang, G.; Chen, M.; Ishaq, M.; Li, X.; Tang, R.; Zheng, Z.; Su, Z.; Fan, P.; Zhang, X.; Chen, S. Crystal Growth Promotion and Defects Healing Enable Minimum Open-Circuit Voltage Deficit in Antimony Selenide Solar Cells. *Adv. Sci.* **2022**, *9*, No.2105142.

(19) Pan, G.; Wang, D.; Gao, S.; Gao, P.; Sun, Q.; Liu, X.; Zhou, Z.; Sun, Y.; Zhang, Y. Substrate Structured Sb_2S_3 Thin Film Solar Cells Fabricated by Rapid Thermal Evaporation Method. *Sol. Energy* **2019**, *182*, 64-71.

(20) Chen, S.; Liu, T.; Chen, M.; Ishaq, M.; Tang, R.; Zheng, Z.; Su, Z.; Li, X.; Qiao, X.; Fan, P.; Liang, G. Crystal Growth Promotion and Interface Optimization Enable Highly Efficient Sb_2Se_3 Photocathodes for Solar Hydrogen Evolution. *Nano Energy* **2022**, *99*, 107417.

(21) Raguse, J. M.; Muzzillo, C. P.; Sites, J. R.; Mansfield, L. Effects of Sodium and Potassium on the Photovoltaic Performance of CIGS Solar Cells. *IEEE J. Photovolt.* **2017**, *7*, 303-306.

(22) Kodalle, T.; Heinemann, M. D.; Greiner, D.; Yetkin, H. A.; Klupsch, M.; Li, C.; van Aken, P. A.; Lauer mann, I.; Schlatmann, R.; Kaufmann, C. A. Elucidating the Mechanism of an RbF Post Deposition Treatment in CIGS Thin Film Solar Cells. *Sol. RRL* **2018**, *2*, No.1800156.

(23) Dharmadasa, I. M. Review of the CdCl_2 Treatment Used in CdS/CdTe Thin Film Solar Cell Development and New Evidence towards Improved Understanding. *Coatings* **2014**, *4*, 282-307.

- (24) McCandless, B. E.; Moulton, L. V.; Birkmire, R. W. Recrystallization and Sulfur Diffusion in CdCl₂-Treated CdTe/CdS Thin Films. *Prog Photovolt Res Appl.* **1997**, *5*, 249-260.
- (25) Chen, P.; Bai, Y.; Wang, S.; Lyu, M.; Yun, J. H.; Wang, L. In Situ Growth of 2D Perovskite Capping Layer for Stable and Efficient Perovskite Solar Cells. *Adv. Funct. Mater.* **2018**, *28*, No.1706923.
- (26) Jiang, Q.; Zhao, Y.; Zhang, X.; Yang, X.; Chen, Y.; Chu, Z.; Ye, Q.; Li, X.; Yin, Z.; You, J. Surface Passivation of Perovskite Film for Efficient Solar Cells. *Nat. Photonics* **2019**, *13*, 460-466.
- (27) Fan, P.; Chen, G. J.; Chen, S.; Zheng, Z. H.; Azam, M.; Ahmad, N.; Su, Z. H.; Liang, G. X.; Zhang, X. H.; Chen, Z. G. Quasi-Vertically Oriented Sb₂Se₃ Thin-Film Solar Cells with Open-Circuit Voltage Exceeding 500 mV Prepared via Close-Space Sublimation and Selenization. *ACS Appl. Mater. Interfaces* **2021**, *13*, 46671-46680.
- (28) Tang, R.; Zheng, Z. H.; Su, Z. H.; Li, X. J.; Wei, Y. D.; Zhang, X. H.; Fu, Y. Q.; Luo, J. T.; Fan, P.; Liang, G. X. Highly Efficient and Stable Planar Heterojunction Solar Cell Based on Sputtered and Post-Selenized Sb₂Se₃ Thin Film. *Nano Energy* **2019**, *64*, No.103929.
- (29) Luo, W.; Calas, A.; Tang, C.; Li, F.; Zhou, L.; Mai, L. Ultralong Sb₂Se₃ Nanowire-Based Free-Standing Membrane Anode for Lithium/Sodium Ion Batteries. *ACS Appl. Mater. Interfaces* **2016**, *8*, 35219-35226.
- (30) Tang, R.; Chen, S.; Zheng, Z. H.; Su, Z. H.; Luo, J. T.; Fan, P.; Zhang, X. H.; Tang, J.; Liang, G. X. Heterojunction Annealing Enabling Record Open-Circuit Voltage in Antimony Triselenide Solar Cells. *Adv. Mater.* **2020**, *34*, No.2109078.
- (31) Duan, H. S.; Yang, W.; Bob, B.; Hsu, C. J.; Lei, B.; Yang, Y. The Role of Sulfur in Solution-Processed Cu₂ZnSn(S,Se)₄ and its Effect on Defect Properties. *Adv. Funct. Mater.* **2013**, *23*, 1466-1471.
- (32) Wang, W.; Wang, X.; Chen, G.; Yao, L.; Huang, X.; Chen, T.; Zhu, C.; Chen, S.; Huang, Z.; Zhang, Y. Over 6% Certified Sb₂(S,Se)₃ Solar Cells Fabricated via In Situ Hydrothermal Growth and Postselenization. *Adv. Electron. Mater.* **2019**, *5*, No.1800683.
- (33) Deng, H.; Yuan, S.; Yang, X.; Zhang, J.; Khan, J.; Zhao, Y.; Ishaq, M.; Ye, W.; Cheng, Y.-B.; Song, H.; Tang, J. High-Throughput Method to Deposit Continuous Composition Spread Sb₂(Se_xS_{1-x})₃ Thin Film for Photovoltaic Application. *Prog Photovolt Res Appl.* **2018**, *26*, 281-290.
- (34) Makreski, P.; Petruševski, G.; Ugarković, S.; Jovanovski, G. Laser-Induced Transformation of Stibnite (Sb₂S₃) and other Structurally Related Salts. *Vib. Spectrosc.* **2013**, *68*, 177-182.

- (35) Deng, Z.; Mansuripur, M.; Muscat, A. J. Simple Colloidal Synthesis of Single-Crystal Sb–Se–S Nanotubes with Composition Dependent Band-Gap Energy in the Near-Infrared. *Nano Lett.* **2009**, *9*, 2015-2020.
- (36) Li, K.; Chen, C.; Lu, S.; Wang, C.; Wang, S.; Lu, Y.; Tang, J. Orientation Engineering in Low-Dimensional Crystal-Structural Materials via Seed Screening. *Adv. Mater.* **2019**, *31*, No.1903914.
- (37) Zhang, H.; Yuan, S.; Deng, H.; Ishaq, M.; Yang, X.; Hou, T.; Shah, U. A.; Song, H.; Tang, J. Controllable Orientations for Sb₂S₃ Solar Cells by Vertical VTD Method. *Prog Photovolt Res Appl.* **2020**, *28*, 823-832.
- (38) Guo, H.; Jia, X.; Hadke, S. H.; Zhang, J.; Wang, W.; Ma, C.; Qiu, J.; Yuan, N.; Wong, L. H.; Ding, J. Highly Efficient and Thermally Stable Sb₂Se₃ Solar Cells based on a Hexagonal CdS Buffer Layer by Environmentally Friendly Interface Optimization. *J. Mater. Chem. C* **2020**, *8*, 17194-17201.
- (39) Liang, G.; Chen, X.; Ren, D.; Jiang, X.; Tang, R.; Zheng, Z.; Su, Z.; Fan, P.; Zhang, X.; Zhang, Y.; Chen, S. Ion Doping Simultaneously Increased the Carrier Density and Modified the Conduction Type of Sb₂Se₃ Thin Films Towards Quasi-Homojunction Solar Cell. *J. Materiomics* **2021**, *7*, 1324-1334.
- (40) Ai, G.; Mo, R.; Xu, H.; Chen, Q.; Yang, S.; Li, H.; Zhong, J. Composition-Optimized TiO₂/CdS_xSe_{1-x} Core/Shell Nanowire Arrays for Photoelectrochemical Hydrogen Generation. *J. Appl. Phys.* **2014**, *116*, No.174306.
- (41) Liang, G.; Liu, T.; Ishaq, M.; Chen, Z.; Tang, R.; Zheng, Z.; Su, Z.; Fan, P.; Zhang, X.; Chen, S. Heterojunction Interface Engineering Enabling High Onset Potential in Sb₂Se₃/CdS Photocathodes for Efficient Solar Hydrogen Production. *Chem. Eng. J.* **2022**, *431*, No.133359.
- (42) Wang, W.; Cao, Z.; Zuo, X.; Wu, L.; Luo, J.; Zhang, Y. Double Interface Modification Promotes Efficient Sb₂Se₃ Solar Cell by Tailoring Band Alignment and Light Harvest. *J. Energy Chem.* **2022**, *70*, 191-200.
- (43) Luo, Y. D.; Tang, R.; Chen, S.; Hu, J. G.; Liu, Y. K.; Li, Y. F.; Liu, X. S.; Zheng, Z. H.; Su, Z. H.; Ma, X. F.; Fan, P.; Zhang, X. H.; Ma, H. L.; Chen, Z. G.; Liang, G. X. An Effective Combination Reaction Involved with Sputtered and Selenized Sb Precursors for Efficient Sb₂Se₃ Thin Film Solar Cells. *Chem. Eng. J.* **2020**, *393*, No.124599.
- (44) Luo, M.; Leng, M.; Liu, X.; Chen, J.; Chen, C.; Qin, S.; Tang, J. Thermal Evaporation and Characterization of Superstrate CdS/Sb₂Se₃ Solar Cells. *Appl. Phys. Lett.* **2014**, *104*, No.173904.
- (45) Wang, W.; Cao, Z.; Wu, L.; Chen, G.; Ao, J.; Luo, J.; Zhang, Y. Interface Etching Leads to the

Inversion of the Conduction Band Offset between the CdS/Sb₂Se₃ Heterojunction and High-Efficient Sb₂Se₃ Solar Cells. *ACS Appl. Energy Mater.* **2022**, *5*, 2531-2541.

(46) Walter, T.; Herberholz, R.; Müller, C.; Schock, H. W. Determination of Defect Distributions from Admittance Measurements and Application to Cu(In,Ga)Se₂ Based Heterojunctions. *J. Appl. Phys.* **1996**, *80*, 4411-4420.

(47) Hu, X.; Tao, J.; Wang, Y.; Xue, J.; Weng, G.; Zhang, C.; Chen, S.; Zhu, Z.; Chu, J. 5.91%-Efficient Sb₂Se₃ Solar Cells with a Radio-Frequency Magnetron-Sputtered CdS Buffer Layer. *Appl. Mater. Today* **2019**, *16*, 367-374.

(48) Li, Y.; Zhou, Y.; Zhu, Y.; Chen, C.; Luo, J.; Ma, J.; Yang, B.; Wang, X.; Xia, Z.; Tang, J. Characterization of Mg and Fe Doped Sb₂Se₃ Thin Films for Photovoltaic Application. *Appl. Phys. Lett.* **2016**, *109*, No.232104.

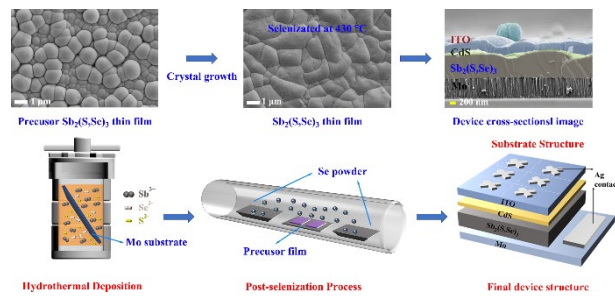
(49) Liang, G. X.; Luo, Y. D.; Chen, S.; Tang, R.; Zheng, Z. H.; Li, X. J.; Liu, X. S.; Liu, Y. K.; Li, Y. F.; Chen, X. Y.; Su, Z. H.; Zhang, X. H.; Ma, H. L.; Fan, P. Sputtered and Selenized Sb₂Se₃ Thin-Film Solar Cells with Open-Circuit Voltage Exceeding 500 mV. *Nano Energy* **2020**, *73*, No.104806.

(50) Herberholz, R.; Walter, T.; Müller, C.; Friedlmeier, T.; Schock, H. W.; Saad, M.; Lux-Steiner, M. C.; Alberts, V. Meyer-Neldel Behavior of Deep Level Parameters in Heterojunctions to Cu(In,Ga)(S,Se)₂. *Appl. Phys. Lett.* **1996**, *69*, 2888-2890.

(51) Kahn, A. Fermi Level, Work Function and Vacuum Level. *Mater. Horizons* **2016**, *3*, 7-10.

(52) Ou, C.; Shen, K.; Li, Z.; Zhu, H.; Huang, T.; Mai, Y. Bandgap Tunable CdS:O as Efficient Electron Buffer Layer for High-Performance Sb₂Se₃ Thin Film Solar Cells. *Sol. Energy Mater. Sol. Cells* **2019**, *194*, 47-53.

(53) Wang, X.; Shi, X.; Zhang, F.; Zhou, F.; Zeng, P.; Song, J.; Qu, J. Chemical Etching Induced Surface Modification and Gentle Gradient Bandgap for Highly Efficient Sb₂(S,Se)₃ Solar Cell. *Appl. Surf. Sci.* **2022**, *579*, No.152193.



TOC